AIAA 81-4012

Evacuation-Induced Pressure Differentials in Multilayer Insulation Systems

A. P. M. Glassford*
Lockheed Palo Alto Research Laboratories, Palo Alto, Calif.

The pressure differentials induced across three types of multilayer insulation systems during evacuation have been measured and compared with values predicted using an idealized parallel plate geometric model. The systems tested were double-aluminized Mylar with a Tissuglas or silk net spacer and crinkled single-aluminized Mylar. Test samples were circular. The influence of purge gas type, layer density, sample diameter, and temperature was systematically investigated. The experimental approach was to measure the absolute pressure history and the corresponding pressure differential induced across the insulation during evacuation. The measured pressure differentials were nondimensionalized and compared with those predicted by the parallel plate model as a function of Knudsen number. It was concluded that the parallel plate model is adequate for making engineering analyses. The influence of all parameters, except layer density, is well represented by the model. Representation of the influence of layer density is less satisfactory, but can be improved by modification of the flat plate model to allow for the more obvious practical nonidealities, such as crinkling, or the presence of a net spacer.

Nomenclature

A = flow passage area
f = specular reflection coefficient
H = flow passage perimeter
h = distance between adjacent insulation layers
Kn = Knudsen number $= \lambda/h$
M = molecular weight
$\dot{m}$ = mass flow rate
N = number of insulation shields per unit thickness
NPD = nondimensionalized pressure differential, defined by Eq. (20)
P = gas pressure between insulation layers
ΔP = gas pressure difference between insulation center and circumference
Q_o = outgassing rate, mass/unit area, unit time
R = gas constant
r = radial position in insulation
T = gas temperature
t = time
t_e = evacuation time constant
v_a = mean molecular velocity $= (8R_oT/\pi M)^{1/2}$
v_o = wall slip velocity
v_r = gas velocity in radial direction
z = coordinate perpendicular to plane of insulation
ρ = gas density
μ = gas viscosity
ϵ = proportionality constant, defined in context
λ = mean free path $= (\pi v_a/4)(\mu/P)$
ξ = slip coefficient
ω_g, ω_w = number of molecular collisions with gas, walls

Subscripts

1,2 = insulation inner, outer radii

Introduction

DURING evacuation of a multilayer insulation (MLI) system, the pressure differentials induced during the high-pressure early part of evacuation can be large enough to deflect permanently or even tear the insulation layers. As the low-pressure region is reached, the MLI material will outgas, and the outgassing rate decay time, in combination with low interlayer flow conductance, will extend the time taken to reach acceptable low pressures. These potential problems can be addressed during design by making a transient gas flow analysis to predict the response of the interlayer gas pressure to the anticipated vacuum chamber or ascent environment pressure history.[1] The simplest geometric model for use in such an analysis is to represent the MLI as a series of smooth parallel plates with a separation distance equal to the reciprocal of the nominal number of shields per unit thickness. Real MLI systems will deviate from this model in various ways. Systems using metallized polymer film shields with glass fiber cloth spacers closely resemble flat plates, but they have no inherent feature to help maintain the same interlayer separation throughout their thickness. Systems with net spacers have relatively much higher lateral stiffness, which helps to establish even spacing, but the net interferes with interlayer flow. Crinkled shield systems also have significant lateral stiffness and thus more even layer spacing, but crinkling produces a variation in interlayer spacing within a given flow channel.

This paper presents the results of a systematic experimental and analytical program[2] to examine the effectiveness with which the evacuation of MLI systems can be predicted using the evenly spaced smooth parallel plate geometric model. In the experimental phase of the program, circular MLI samples were evacuated in a vacuum chamber. Circular specimens were used so as to eliminate net pressure forces and to avoid the need for sealing any edges. The pressure in the chamber and the induced pressure differential between the center and circumference of the insulation samples were measured as functions of time. Tests were conducted with different types of insulation, while sample diameter, number of layers per unit thickness, purge gas type, and temperature were systematically varied. In the analytical phase of the program, a transient flow analysis was made by applying continuity and momentum equations to a model based on equally spaced flat circular plates with radial flow. The effectiveness of the model was evaluated by comparing the pressure differentials predicted by the model with the experimentally measured values. To simplify the task of evaluation, the data were reduced to nondimensional form. The pressure differential data are expressed in the form of a nondimensional pressure differential (NPD), defined in the text, and are presented as a function of instantaneous absolute pressure, expressed in the form of Knudsen number.

Received Jan. 29, 1980; revision received June 5, 1980.

*Staff Scientist, Material Sciences Laboratory. Member AIAA.

In real MLI systems, outgassing strongly influences the interlayer pressure history. However, the flow conductance properties of the MLI, which are the subject of the present study, are not affected by the presence of outgassing. The influence of outgassing was therefore irrelevant to the study, and so this effect was systematically excluded. In the experimental phase, this was done by preevacuating the MLI test systems before beginning the measurement program, so as to remove most of the sorbed species. The subsequent evacuation tests were then terminated at pressures sufficiently high for the residual outgassing rate to be insignificant. In the theoretical phase, the mass generation term in the continuity equation was simply set equal to zero. When the model is used to predict the pressure history in a real MLI system, outgassing can be accounted for by setting this mass generation term equal to experimentally obtained outgassing rate data for the appropriate MLI materials and conditions.

Experimental Program

Apparatus

Preparation of MLI Test Systems

Table 1 gives the specifications of the MLI materials used, while Table 2 gives the dimensions and other parameters for the systems tested. The double-aluminized Mylar/Tissuglas, double-aluminized Mylar/silk net, and crinkled single-aluminized Mylar systems are referred to in this paper as DAM/TG, DAM/SN, and CSAM, respectively.

Layers of insulation materials were cut in circular form. Most layers were cut 68.6 cm in diameter. The exceptions were the 50.8-cm- and the 38.1-cm diam layers used in tests to investigate the effect of flow path length. A hole 0.32-cm in diam was made in the center of each layer. The test systems were prepared by stacking the layers in the appropriate manner for each MLI type. The DAM/TG systems were composed of alternate layers of these materials with the first and last layers both being Tissuglas spacers. For the DAM/SN systems, two layers of net were used between successive shields, and the outer layers were both shields. The CSAM system was stacked with all layers oriented the same way with respect to the metallized and unmetallized sides. The total number of shields in all test samples were either 20 or 80.

MLI Test System Holder

Figure 1 is a schematic drawing of the apparatus. The MLI test systems were held between two circular aluminum plates. The plates were bolted together using appropriately sized spacers between the plates to maintain the required nominal shield layer density for each test. Copper coils were bonded to the outer surfaces of the plates to enable them to be cooled by liquid nitrogen. A Barocel diaphragm-type differential pressure sensor of 10-Torr (1.3×10^3 Pa) capacity was mounted on low-thermal conductance supports about 15 cm above the center of the upper plate. A tube connected the measuring side of the sensor to a central hole in the upper boundary plate, which lined up with the central hole in the MLI test system layers. A tube of equivalent flow resistance was attached to the reference side of the pressure sensor, with its free end open to the vacuum chamber, to compensate for the pressure differential induced in the tubing between the measuring side of the sensor and the center of the MLI due to evacuation of the sensor void volumes. It was assumed that the pressure difference in the vacuum chamber between the circumference of the insulation and the end of the pressure sensor reference side compensator tube was at all times negligible. The sensor output was thus assumed to be equal to the true pressure difference between the center of the insulation and its outer edge.

Vacuum Chamber

The MLI test system holder was suspended in the center of a cylindrical vacuum chamber by four stainless steel rods attached to its removable lid. The vacuum chamber was approximately 76 cm in diameter and 56 cm deep. It could be evacuated by a mechanical pump to pressures near 0.02 Torr (2.7 Pa) in 2-3 min, and could be diffusion-pumped to pressures below 10^{-5} Torr (1.3×10^{-3} Pa). The chamber pressure was measured by a system of two parallel Barocel differential pressure sensors mounted outside the vacuum chamber. These sensors had capacities of 1000 and 10 Torr (1.3×10^5 and 1.3×10^3 Pa), respectively, and allowed accurate measurement of chamber pressure from 1 atm down to approximately 10^{-4} Torr (1.3×10^{-2} Pa). Their reference sides were connected to a separate diffusion pumping system, which maintained the reference pressure below the negligible value of 10^{-6} Torr (1.3×10^{-4} Pa). Chamber pressures below 10^{-4} Torr (1.3×10^{-2} Pa) were measured using an ionization gage system.

Nitrogen, argon, and helium gas supply systems were available for repressurizing the chamber.

Barocel Differential Pressure Sensors

Barocel sensors must be periodically zeroed by equalizing the pressures on each side of the diaphragm and adjusting an ac bridge network to give zero output for this condition. The two vacuum-chamber absolute pressure sensors were zeroed by using provided valving to connect their measuring and reference ports together. For the insulation pressure differential sensor, zeroing was performed with the chamber evacuation valve closed so that the pressure throughout the insulation and chamber, and hence on both sides of the sensor, would be essentially uniform. It was impossible to zero the sensors during the evacuation tests because of their short duration. Instead, the sensors were zeroed only before

Table 1 Insulation material specifications

Designation	Use	Source	Nominal thickness, mm	Nominal specific weight, $kg/m^2\times10^{-3}$
Unperforated, double-aluminized 0.0064-mm Mylar	Shield	National Metallizing Div., Standard Packaging Corp., Cranbury, N.J.	0.0064	8.8
Crinkled, single-aluminized 0.0064-mm Mylar	Shield with integral spacer	National Metallizing Div., Standard Packaging Corp., Cranbury, N.J.	0.0064	9.3
Illusion silk net, approx. 0.159-cm hexagonal mesh	Spacer	John Heathcoat Co., New York, N. Y.	0.13	7.3
Tissuglas, style 60G	Spacer	Pallflex Products Co., Putnam, Conn.	0.014	3.9

evacuation with the pressure at 1 atm. For sensors zeroed at the high-pressure end of their range, the manufacturer specifies an accuracy of 0.1% of the reading plus 0.01% of the sensor full range, giving a limiting low-pressure accuracy of the order of ±0.001 Torr (0.13 Pa) for the 10 Torr (1.3×10^3 Pa) sensor. In the present tests, this error appeared in the data in the form of systematically low readings at low absolute pressures.

Test Procedure

Table 2 lists the various combinations of the MLI system, layer density, sample diameter, purge gas type, and temperature that were tested.

Whenever a new MLI sample was placed in the chamber, or if the chamber and sample had been otherwise exposed to the atmosphere, the system was preconditioned by diffusion-pumping for 24 h to reduce the outgassing rate to a negligible amount. The chamber was then back-filled with the purge gas to be used in the next test. Thus, each evacuation test began with the sample preconditioned and immersed in a 1-atm environment of argon, helium, or nitrogen.

An evacuation test consisted of zeroing the pressure sensors, opening the valve to the mechanical pump, and recording the analog output from the absolute chamber pressure and the MLI differential pressure sensors on strip chart recorders. During the evacuation, both absolute and differential pressures decreased by several orders of magnitude; the sensor output ranges were therefore changed periodically so that an adequately high input voltage to the recorder could be maintained. Also, when the chamber pressure fell below 10 Torr (1.3×10^3 Pa), the recorder was switched manually from the 1000-Torr (1.3×10^5 Pa) sensor to the 10-Torr (1.3×10^3 Pa) sensor. The mechanical pump reduced the chamber pressure exponentially down to about 0.03-0.02 Torr (4.0-2.7 Pa) in about 2 min. Below this pressure, the evacuation rate slowed significantly, due partially to the increasing significance of residual outgassing. The test was terminated at this point because the selected method of data reduction, to be described later, required an exponential pressure history and zero outgassing. Also, at this pressure level, the evacuation flow was well enough into the free-molecule regime to produce an adequate range of data. The chamber was then repressurized to 1 atm with the appropriate purge gas for the next test. All evacuations were repeated at least once. Pressure data for a given time in an evacuation, obtained in repeated evacuations, generally agreed to within ±3%.

In the tests made at temperatures below 298 K, the MLI test system was cooled before evacuation by passing liquid nitrogen through the coils on the boundary plates. During this process, the purge gas enhanced heat transfer from the MLI to the plates, but it also caused cooling of the chamber walls and other structural components as well as resulting in a greater mass of gas in the chamber at the beginning of evacuation. Consequently, the chamber evacuation rate was slower than for the 298 K tests, but it remained exponential for the early part of evacuation. At later times, the rate became increasingly less exponential because of rewarming of the chamber. For the DAM/SN tests, a relatively long time

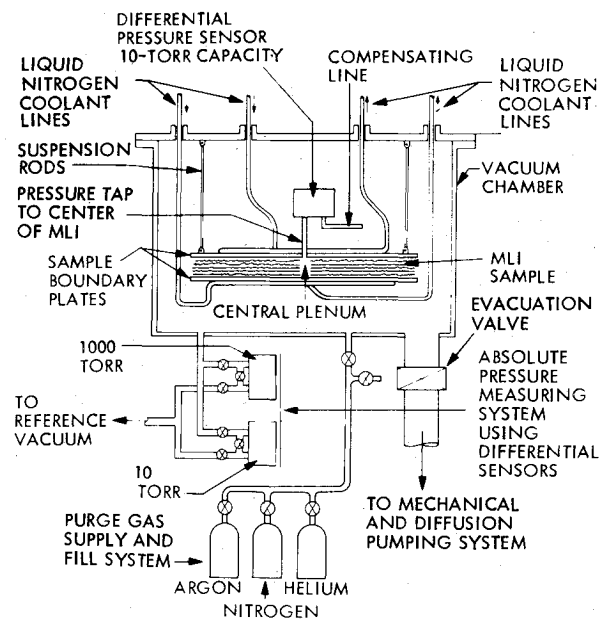

Fig. 1 Schematic of apparatus.

Table 2 Schedule of evacuation tests

Type of insulation	Sample code	Sample, diam, cm	Total no. of shields	Boundary plate separation, cm	Shield layer density, no./cm	Test temp, K	Purge gas species
Double-aluminized Mylar/Tissuglas (DAM/TG)	1A	68.6	20	0.406	46.8[a]	298	He,N_2,A
	1B	68.6	20	0.348	54.7[a]	298	He,N_2,A
	1C	68.6	20	0.229	83.0[a]	298	He,N_2,A
	2	50.8	20	0.348	54.7[a]	298	N_2
	3	38.1	20	0.348	54.7[a]	298	N_2
	4	68.6	80	1.392	56.8[a]	128, 182	He
	4	68.6	80	1.392	56.8[a]	213, 239	He
	4	68.6	80	1.392	56.8[a]	287, 298	He
Double-aluminized Mylar/double silk net (DAM/SN)	5A	68.6	20	0.742	28.4[b]	298	N_2
	5B	68.6	20	0.544	38.6[b]	298	N_2
	5C	68.6	20	0.442	47.5[b]	298	N_2
	6	50.8	20	0.544	38.6[b]	298	N_2
	7	38.1	20	0.544	38.6[b]	298	N_2
	8	68.6	80	2.098	38.6[b]	131, 266	He
	8	68.6	80	2.098	38.6[b]	272, 276	He
	8	68.6	80	2.098	38.6[b]	298	N_2,He,A
Crinkled single-aluminized Mylar (CSAM)	9A	68.6	20	0.726	28.9	298	N_2
	9B	68.6	20	0.597	35.2	298	N_2
	9C	68.6	20	0.363	57.9	298	N_2

[a] Values shown correspond to specimens with one less spacer layer than the number of shields shown. [b] Values shown correspond to specimens with one more spacer layer than the number of shields shown.

was allowed for attainment of thermal equilibrium before making an evacuation, which resulted in significant cooling of the chamber. During subsequent evacuation, the departure from exponential behavior occurred as early as 0.8 min after beginning evacuation. For the DAM/TG tests, a shorter time was allowed for temperature equilibrium to be attained before evacuation was begun, and minimal deviation from exponential behavior was found.

Typical Data

The full body of experimental data is tabulated in Ref. 2. It has been nondimensionalized and presented in the Results and Discussion section of this paper. The form of the basic experimental data is the same for all tests and can be shown with a single typical example. Figures 2a and 2b show the recorded absolute and differential pressure histories, respectively, for evacuation of helium from double-aluminized Mylar/Tissuglas, 298 K sample, test 4. Figure 2a shows the absolute-pressure sensor scale switching points as well as the discontinuity caused by the change from the 1000 Torr (1.3×10^5 Pa) sensor to the 10 Torr (1.3×10^3 Pa) sensor. When these data are processed, an exponential pressure history is obtained for most of the pressure range above about 0.03 Torr (4 Pa). This is because the chamber was evacuated by a mechanical pump, which, for the most of its pressure range, induces a more or less fixed volume of gas per stroke from a constant volume chamber, regardless of gas species. A

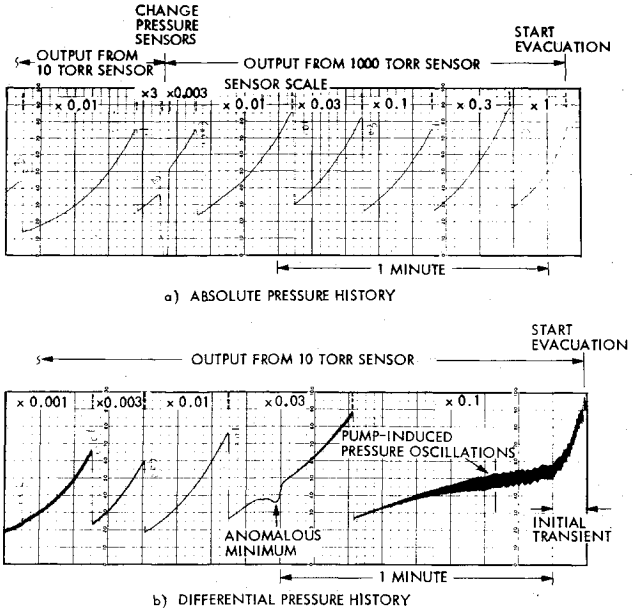

Fig. 2 Typical experimental strip-chart data. a) absolute pressure history; b) differential pressure history. Data are for evacuation of helium from DAM/TG sample 4 at 300 K.

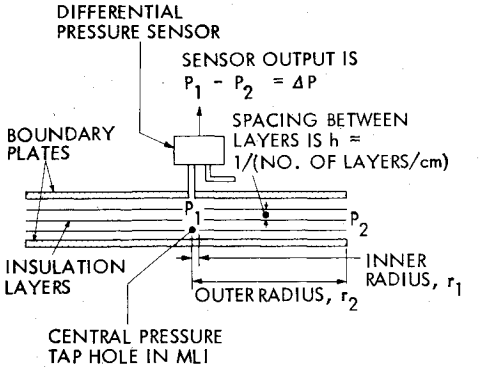

Fig. 3 Idealized model used in the theoretical analysis.

slightly higher rate of pressure reduction is measured in the first few seconds of evacuation because of the capacity of the evacuation line between valve and pump. Below about 0.03 Torr (4 Pa), various effects begin to limit the capacity of the mechanical pump, and a decreasing rate of evacuation is obtained. The chamber pressure history can be represented by $P=1\times10^6\exp(-t/t_e)$ Pa, with t in min. For argon, the time constant t_e was 0.20 min, while for helium and nitrogen it was 0.21 min. For those tests on samples 4 and 8 at temperatures lower than 298 K, the evacuation time constant was longer. It varied in the range of 0.21-0.30 for the portion of the evacuation that remained exponential.

The differential pressure trace on Fig. 2b shows the higher initial pressure differential in response to the initial higher rate of pressure decay previously noted. Thereafter, in response to the exponential chamber pressure history, the pressure differential has a relatively constant value in the continuum regime, changing to an exponential time dependence in the free-molecule regime. In the example shown, the constant pressure differential region is very brief. For MLI systems with wider spacings between layers, the flow remains in the continuum regime for a longer time so that the constant pressure differential regime also persists for a longer time. The response of the pressure sensor to the pressure oscillations produced in the chamber by the reciprocating vacuum pump in the continuum regime is apparent. In the region of transition from continuum to free-molecule flow, a minimum in the pressure differential is indicated. This minimum was present in all evacuations and was most marked for helium and least marked for argon. Since it was also present with no MLI sample in place, it is assumed to be produced by the pressure measuring system, possibly by flow transition phenomena in the sensor porting and connecting tube system.

Theory

Model

The MLI systems tested are modeled as a stack of flat circular plates. Because the central hole equalizes the pressure at the center of each layer, the stack consists of a series of identical parallel radial flow paths, which can be analyzed by considering flow between a single adjacent pair of circular plates. Figure 3 shows such a model. In an actual insulation system, the radius of the central hole r_1 is very small compared to r_2 and is assumed to be zero in the analysis.

Continuity Equation

Because of the uniform pressure around the circumference of the MLI, flow will be axisymmetric. Since $r_2 \gg h$, flow in the z direction can be neglected. The continuity equation can then be written as follows:

$$-\frac{d\rho}{dt}=\frac{1}{r}\frac{\partial}{\partial r}(\rho r\bar{v}_r)-\frac{2Q_o}{h} \tag{1}$$

where $\bar{v}_r$ is the average flow velocity across the interlayer space at radius r. For a perfect gas and negligible outgassing rate, Eq. (1) becomes

$$-\frac{dP}{dt}=\frac{1}{r}\frac{\partial}{\partial r}(Pr\bar{v}_r) \tag{2}$$

Momentum Equation

During evacuation, the flow regime passes from viscous through transitional to free-molecule flow. Momentum relationships in the viscous regime and the high-pressure end of the transition regime can be represented by the Navier-Stokes equations, modified to include slip flow. In the free-molecule regime, Knudsen's equation applies. Because of the different phenomena represented by these basic equations, it is not possible to derive from physical principles a single

momentum equation valid in all flow regimes. Instead, expressions are derived for $\bar{v}_r$ for each flow regime and are then combined empirically.

The Navier-Stokes equations for axisymmetric radial flow and negligible flow in the z direction are

$$-\frac{dP}{dr}+\mu\frac{\partial^2 v_r}{\partial z^2}=0 \tag{3}$$

Equation (3) can be integrated with respect to z with the boundary conditions $\partial v_r/\partial z=0$ at $z=h/2$, and $v_r=v_o$ at $z=0,h$. The velocity distribution is then

$$v_r=\frac{-1}{2\mu}[hz-z^2]\frac{dP}{dr}+v_o \tag{4}$$

v_o is the slip velocity, equal to zero for pure viscous flow. The shear stress at the passage walls is set equal to v_o times a constant ϵ. By definition, the shear stress is also equal to $\mu(\partial v_r/\partial z)$ at the wall. Hence,

$$v_o\epsilon=\frac{-h}{2}\frac{dP}{dr} \tag{5}$$

Equations (4) and (5) can be combined and integrated to give $\bar{v}_r$

$$\bar{v}_r=-\frac{h^2}{12\mu}\left[1+\frac{6\mu}{\epsilon h}\right]\frac{dP}{dr} \tag{6}$$

The ratio μ/ϵ is the slip coefficient ζ and is given by [3]

$$\frac{\mu}{\epsilon}=\zeta=\frac{\mu}{P}\cdot\frac{\pi v_a}{4}\cdot\frac{2-f}{f} \tag{7}$$

where f is the specular reflection coefficient, equal to the fraction of molecules incident on a channel wall which are reflected diffusely.

Combining Eqs. (6) and (7) gives

$$\bar{v}_r=-\frac{h^2}{12\mu}\left[1+\left(\frac{6\mu}{Ph}\right)\cdot\left(\frac{\pi v_a}{4}\right)\cdot\left(\frac{2-f}{f}\right)\right]\frac{dP}{dr} \tag{8}$$

Equation (8) can be rewritten in terms of Kn to give an expression for $\bar{v}_r$ valid in the continuum and slip flow regimes

$$\bar{v}_r=-\frac{h}{12\mu}\left[1+6\frac{(2-f)}{f}Kn\right]\frac{dP}{dr} \tag{9}$$

In the free-molecule flow regime, the relationship between mass flow and pressure drop is given by Knudsen's equation.[4]

$$\dot{m}=\frac{4}{3}\frac{v_a}{RT}\frac{A^2}{H}\frac{dP}{dr} \tag{10}$$

where A and H are equal to $2\pi rh$ and $4\pi r$, respectively, for radial flow. The mean velocity in free-molecule flow for a perfect gas is thus

$$\bar{v}_r=\frac{2h}{3P}\cdot v_a\cdot\frac{dP}{dr} \tag{11}$$

Equation (11) can be rewritten as follows:

$$\bar{v}_r=\frac{-h^2}{12\mu}\left[\frac{32}{\pi}Kn\right]\frac{dP}{dr} \tag{12}$$

Browne and John[5] describe a method for combining Eq. (9) and Eq. (12) into a single expression for $\bar{v}_r$ which transforms from Eq. (9) to Eq. (12) smoothly and exactly as the Knudsen number increases. The continuum slip flow analysis is based upon intermolecular collisions, whereas Knudsen's equation was derived assuming that gas molecules collide only with the passage walls. The relative validity of the two equations is then assumed to be proportional to the ratio of the number of collisions with other molecules ω_g to the number of collisions with the passage walls ω_w. Browne and John show that

$$\frac{\omega_g}{\omega_g+\omega_w}=\frac{2/Kn}{1+2/Kn} \tag{13}$$

They also suggest the reasonable assumption that $f=0.857$, permitting the factor $(2-f)/f$ to be rounded off to 4/3. An equation for $\bar{v}_r$ valid in all flow regimes can now be written as

$$\bar{v}_r=\frac{-h^2}{12\mu}\left[1+\left(\frac{2/Kn}{1+2/Kn}\right)8Kn+\left(\frac{1}{1+2/Kn}\right)\frac{32Kn}{\pi}\right]\frac{dP}{dr} \tag{14}$$

The three terms in the parenthesis in Eq. (14) relate to viscous, slip, and free-molecule flow, respectively. The slip flow and free-molecule flow terms are multiplied by factors obtained from Eq. (13), expressing their relative significance as a function of Kn. Equation (14) can be consolidated to give

$$\bar{v}_r=\frac{-h^2}{12\mu}\left[1+\frac{32Kn}{\pi}\left(\frac{1+\pi/2Kn}{1+2/Kn}\right)\right]\frac{dP}{dr} \tag{15}$$

Solution of the Equations

The general equation for the pressure in the MLI is obtained by substituting Eq. (15) into Eq. (2), which produces a nonlinear second-order partial differential equation in pressure as a function of time and radius. In Ref. 2, a simple Newtonian method was used to obtain solutions for the MLI systems and conditions of this paper. For most of the evacuation, these solutions indicated that, for the specific systems considered, the variation of pressure through the MLI at any given point in time was small compared to the instantaneous absolute pressure. With this knowledge, the continuity equation can be simplified and a closed-form nondimensionalized solution for pressure differential can be obtained. This greatly simplifies the task of comparing theory and experiment.

If it can be assumed that $(\partial P/\partial r)\ll P/r$, then Eq. (2) can be rewritten as

$$-\frac{\partial P}{\partial t}=\frac{P}{r}\cdot\frac{\partial(\bar{v}_r r)}{\partial r} \tag{16}$$

Substituting Eq. (15) in Eq. (6) and rearranging gives

$$\left(\frac{1}{P}\frac{\partial P}{\partial t}\right)r\,dr=\frac{\partial}{\partial r}\left[\frac{-h^2 r}{12\mu}\left(1+\frac{32Kn}{\pi}\left(\frac{1+\pi/2Kn}{1+2/Kn}\right)\right)\frac{\partial P}{\partial r}\right]dr \tag{17}$$

If the pressure history during evacuation is exponential, the factor $[1/P(dP/dt)]$ is constant and equal to $-1/t_e$. Hence, Eq. (17) can be integrated with respect to r to give

$$-\frac{r}{2t_e}=\frac{h^2}{12\mu}\left(1+\frac{32Kn}{\pi}\left(\frac{1+\pi/2Kn}{1+2/Kn}\right)\right)\frac{\partial P}{\partial r}+(\text{const}) \tag{18}$$

$\partial P/\partial r = 0$ when $r = r_1 = 0$, so the constant of integration disappears from Eq. (18). Integration of Eq. (18) with respect to r gives

$$\frac{r_2^2}{4t_e} = \frac{h^2}{12\mu}\left(1 + \frac{32Kn}{\pi}\left(\frac{1+\pi/2Kn}{1+2/Kn}\right)\right)\cdot\Delta P \qquad (19)$$

The nondimensional pressure drop (NPD) is defined as follows:

$$\text{NPD} = \frac{\Delta P h^2 t_e}{\mu r_2^2} \qquad (20)$$

Equation (19) can now be rewritten in nondimensional form as

$$\text{NPD} = \frac{3}{1 + \frac{32Kn}{\pi}\left(\frac{1+\pi/2Kn}{1+2/Kn}\right)} \qquad (21)$$

Results and Discussion

The experimental data have been nondimensionalized in accordance with the theory derived in the previous section. Absolute and differential pressure data were taken from the strip chart recordings at intervals of 0.1 min. The NPD was calculated from Eq. (20) using the experimental pressure history data, the appropriate sample dimensions, and purge gas viscosity and molecular weight. The experimental absolute and differential pressures were averaged to determine their values midway between the 0.1-min intervals. For the DAM/SN and CSAM systems, h was assumed to be equal to the mean spacing between shields, less the material thickness. In the DAM/TG system, the Tissuglas spacer constitutes another flow boundary, so h was assumed to be half the mean distance between shields. Kn was calculated for corresponding points in time from h, gas property data, and the average absolute pressure.

Figures 4-14 show the NPD as a function of Kn, along with the theoretical relationship [Eq. (21)]. In some figures, increasing scatter and systematic deviant trends are observed at the highest values of Kn, i.e., at the lowest pressures. These trends are due to the increasing significance of the zero error in the pressure sensors noted in the description of the apparatus. The effectiveness of the flat plate model is now assessed by considering each variable in turn.

Purge Gas Type

Figures 4-7 show the NPD vs Kn for evacuation of nitrogen, argon, and helium from the DAM/TG systems 1A, 1B, and 1C and DAM/SN system 8. The nondimensional data for each gas species lie on a single experimental characteristic for a given sample. It is concluded that the influence of purge gas type is correctly modeled by the idealized theory.

Sample Diameter

Figures 8 and 9 show data for evacuation of nitrogen from the DAM/TG systems 1B, 2, and 3 and the DAM/SN systems 5B, 6, and 7, respectively. For each material, the nondimensional data for the three diameters lie on single experimental characteristics. It is concluded that the effect of diameter is correctly modeled by the idealized theory.

MLI Type and Layer Density

Figures 10-12 show the NPD vs Kn for the evacuation of nitrogen from the three MLI systems at three layer densities. Figure 10 was obtained by plotting the nitrogen data from Figs. 4-6. A similar characteristic would have been obtained had the helium or argon data from Figs. 4-6 been used for the comparison. The model is clearly less able to represent layer

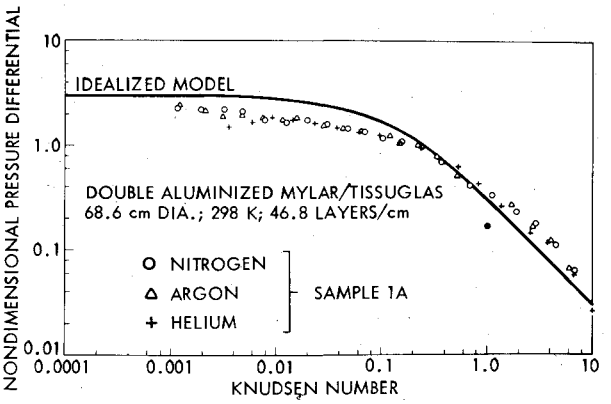

Fig. 4 Effect of purge gas species; DAM/TG, 46.8 layers/cm.

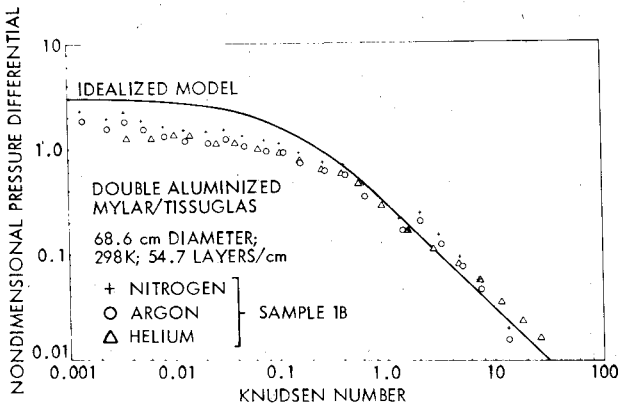

Fig. 5 Effect of purge gas species; DAM/TG, 54.7 layers/cm.

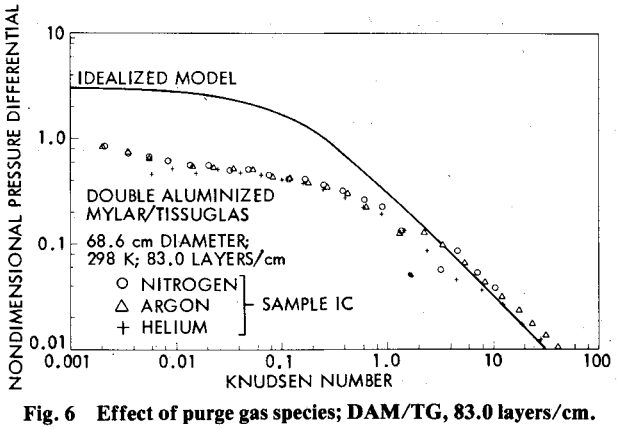

Fig. 6 Effect of purge gas species; DAM/TG, 83.0 layers/cm.

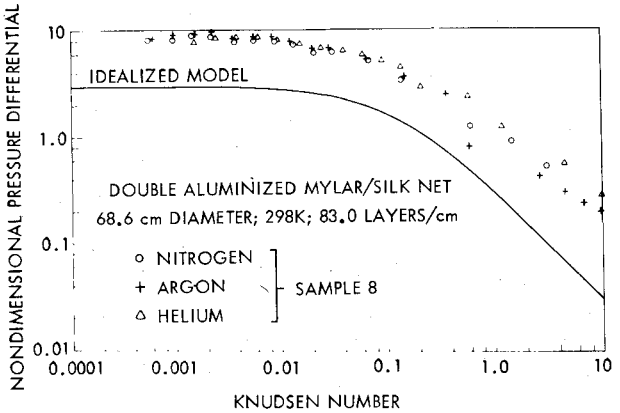

Fig. 7 Effect of purge gas species; DAM/SN.

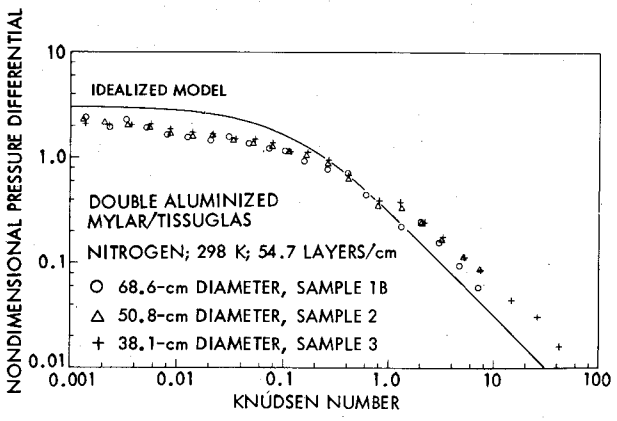

Fig. 8 Effect of sample diameter; DAM/TG.

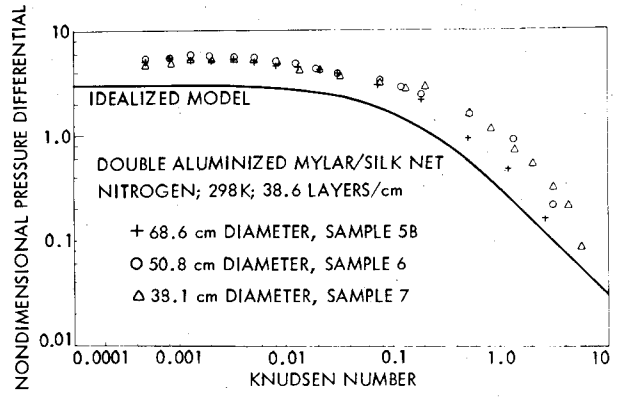

Fig. 9 Effect of sample diameter; DAM/SN.

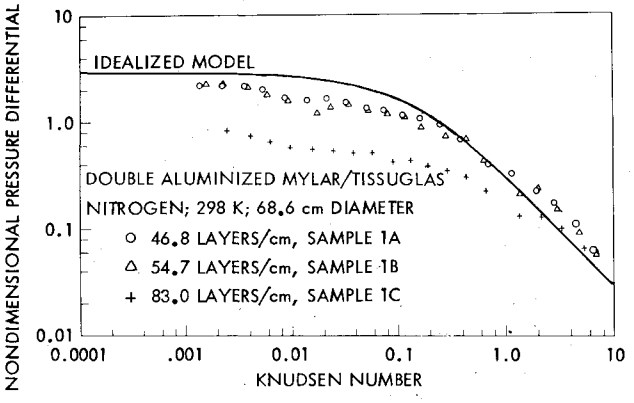

Fig. 10 Effect of layer density; DAM/TG.

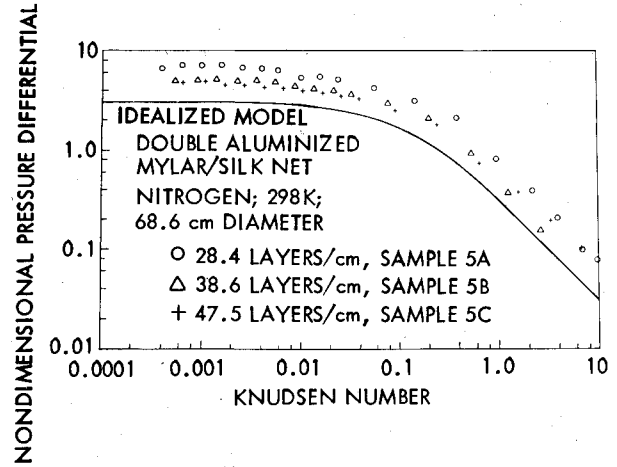

Fig. 11 Effect of layer density; DAM/SN.

density than either purge gas type or diameter. Three general trends are evident. First, correlation with the theory is better in the free-molecule regime than in the viscous regime. Second, in the viscous regime, the experimental NPD seems to fall with increasing shield layer density. This pattern is seen for each MLI system individually and also from system to system. Third, the DAM/SN and CSAM NPD data lie above the theoretical NPD characteristic, while the DAM/TG data lie below.

The observed differences between the experimental and theoretical NPD result almost certainly from the two main differences between real MLI systems and the model. In real systems, the spacing between adjacent layers will not be equal to the mean value, but will have a distribution of values about this mean. Also, the flow passage may be partially blocked (e.g., by netting), or its walls may be irregular. It is shown in the Appendix that uneven layer spacing would tend to reduce the pressure drop relative to the evenly spaced value. On the other hand, blockage of the interlayer flow passage, or crinkling of the walls, would clearly increase the passage flow resistance above the smooth, flat-walled value.

When one examines the data in view of these considerations, it would be inferred that the flow passages in the DAM/TG system are relatively smooth and flat, like the model. On the other hand, even at the highest layer density of 83 shields/cm, the mean spacing between shields is 0.12 mm, whereas the combined thickness of one shield and one spacer is only 0.0213 mm. The thickness of the materials is thus insufficient to maintain even spacing of the shields at this density, so this system seems to be susceptible to uneven layer spacing. As shown in the Appendix, this would result in lower-than-theoretical pressure differentials, which is in accordance with the observed behavior.

For DAM/SN, the combined thickness of one shield plus the maximum thickness of two layers of net is 0.266 mm. This is almost adequate to establish the interlayer separation positively, even at the lower layer density of 28.4 layers/cm, for which the mean spacing is 0.35 mm. At the highest density of 47.5 layers/cm, where the mean spacing is 0.21 mm, some packing of the net is required. For the CSAM, the lowest layer density of 28.9 layers/cm corresponds to a mean spacing of 0.35 mm. Although no specification exists for the degree of crinkling, inspection of the material indicates crinkling heights of at least 0.50 mm, which should be enough to establish the desired layer density. For both DAM/SN and CSAM, the interlayer density should thus be fairly evenly maintained by the dimensions of the materials, and the reduction in pressure differential due to uneven spacing should be minimal. However, the flow channels will be clearly more obstructed and irregular than those of the model, and the resulting increase in pressure differential could be significant. This also is in accordance with the observed behavior. The magnitude of the additional flow passage resistance caused by the net spacer in the DAM/SN system

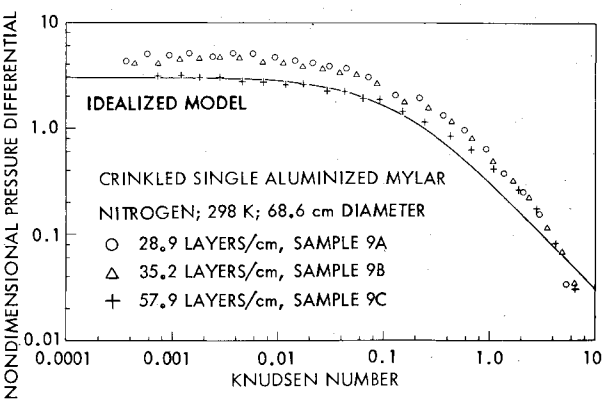

Fig. 12 Effect of layer density; CSAM.

can be estimated for the viscous regime with the use of the concept of effective hydraulic diameter d_h, equal to (4 × free volume of passage/wetted surface area). For the unobstructed space between flat plates, d_h is equal to $2h$. The silk net had about 38 cells/nominal cm^2, each incorporating about 0.56 cm of silk fiber of about 0.004 cm diam. The surface area and volume per nominal cm^2 of the two silk net spacers are thus about 0.53 cm^2 and 5.3×10^{-4} cm^3, respectively. The hydraulic diameter is thus equal to $4\times(h-5.3\times10^{-4})/(2+0.53)$. In all cases, $h\gg5.3\times10^{-4}$, so the effective value of d_h is 1.58 h. This corresponds to an effective reduction in h to about 0.8 h. Since the NPD is proportional to $1/h^2$, the effect of flow passage blockage is apparently of the right order of magnitude to explain the higher-than-theoretical measured NPD values.

For the CSAM system, the crinkling will result in variable layer separation in the radial direction with local values lying between zero and $2h$. Such a flow path will have a higher flow resistance than a parallel-sided path of width. However, it is not possible to estimate the magnitude of the effect of crinkling in a simple manner because of its random nature.

Temperature

Figures 13 and 14 show the NPD as a function of *Kn* for evacuation of helium from DAM/TG system 4 and DAM/SN system 8, respectively, at different temperatures. The DAM/TG data show poorer correlation at low *Kn*, improving to relatively good correlation at higher *Kn*. The DAM/SN data show good correlation at low *Kn*, worsening as *Kn* increases.

The main possible causes of the differences between the theoretical and experimental NPD are incorrect temperature measurement and nonexponential evacuation rate. Analysis of possible errors in temperature measurement indicates that these would be insufficient to explain the regions of poor correlation.

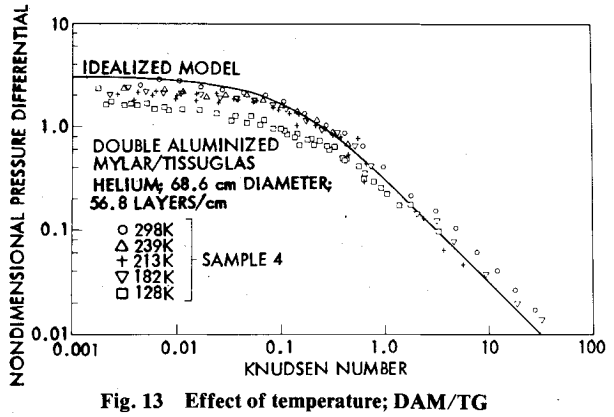

Fig. 13 Effect of temperature; DAM/TG

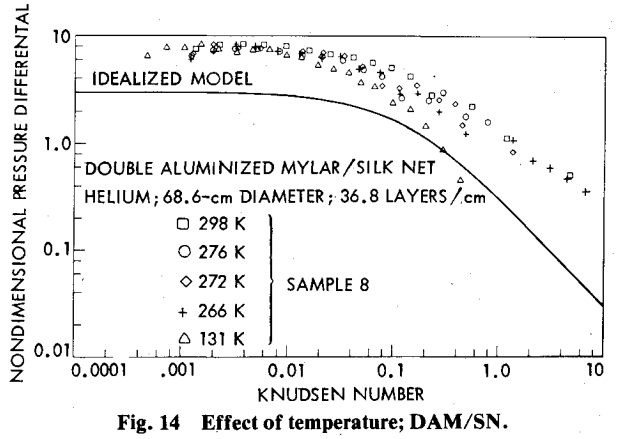

Fig. 14 Effect of temperature; DAM/SN.

For the DAM/SN, the most probable reason for the increasing scatter of the data with increasing *Kn* is that the chamber pressure history became increasingly nonexponential toward the later stages of evacuation, as noted in the section on Test Procedure. Since the chosen method of nondimensionalizing the data requires that $1/P\cdot dP/dt$ be constant throughout an evacuation, deviation from this condition will necessarily reduce the degree of correlation. In the DAM/TG tests, the pressure histories varied little from exponential form, and no noticeable increase in scatter is observed in the later stages of evacuation.

For the DAM/TG system, the general level of agreement between experiment and theory with varying *Kn* is similar in character to that found for the 300 K tests on this system. It is therefore concluded that the differences between the experimental and theoretical NPD in Fig. 13 could result mainly from uneven layer spacing, as discussed earlier. The effect of temperature is concluded to contribute minimally to these differences, and thus appears to be satisfactorily represented by the model.

Conclusions

It appears that the evacuation of the MLI systems can be predicted with an accuracy adequate for engineering design studies by modeling them as a series of parallel flat plates. The influence of purge gas type and flow path length is well represented by the model. The effect of temperature also appears to be adequately modeled, but this was less conclusively established because of minor problems in experimental technique. The major weakness of the model lies in the representation of MLI layer density, inasmuch as uneven layer spacing and channels with irregular walls or partially obstructed flow are not accounted for. Evaluation of the evacuation behavior of a practical MLI system, assuming even spacing, will lead to a high estimate of pressure differential for those systems susceptible to uneven layer separation. This situation should be acceptable for engineering purposes. Also, the effect of uneven spacing on the pressure differential should be less in most practical systems where there is no flow communication between layers. For systems with rough or obstructed flow passages, the actual pressure differentials will be higher than the predicted values, which is undesirable from an engineering analysis standpoint. However, this defect is not serious, and the model appears to be modifiable to account for these features by estimating the effective hydraulic diameter of the irregular flow passage.

The specific theory presented in this paper was developed to enable measured pressure differentials to be compared with the theoretical predictions for the particular experimental configuration studied. The theory is directly applicable to evacuation of any other circular system where the evacuation rate is exponential. For other one-dimensional flow situations, Eq. (15) for $\bar{v}_r$ is applicable, but the continuity equation must be rewritten for the geometry of interest. For multidimensional flow, the average flow velocity expression must also be rederived. Also, in all practical applications, the effect of outgassing sould be included by giving an appropriate value of Q_o in Eq. (15).

Appendix: Influence of Variable Layer Density

In an evenly spaced situation, each channel has a width of h. If the middle layer separating two adjacent channels is displaced, Δh to one side, with the two outer layers maintaining the same relative positions, then the interlayer separations will become $(h+\Delta h)$ and $(h-\Delta h)$. For the same evacuation rate, the total mass flow rate from the two spaces must be the same before and after displacement of the center layer. If v_{r1}, v_{r2+}, and v_{r2-} are the mean flow velocities at any insulation radius r for the initial evenly spaced situtation and the wider and narrower channels in the uneven situation,

respectively, then equating mass flow rates at this radius gives

$$2(2\pi rh)\cdot\rho\bar{v}_{r1} = (2\pi r(h+\Delta h))\rho\bar{v}_{r2} + (2\pi r(h-\Delta h))\rho v_{r2-} \tag{A1}$$

The pressure differentials for the evenly and unevenly spaced situations are denoted by ΔP_1 and ΔP_2, respectively. Noting that in the viscous regime $\bar{v}_r$ is proportional to $h^2\Delta P$ [Eq. (15)], Eq. (A1) can be rewritten as

$$2h^3\Delta P_1 = [(h+\Delta h)^3 + (h-\Delta h)^3]\Delta P_2 \tag{A2}$$

so

$$\frac{\Delta P_2}{\Delta P_1} = \frac{1}{1+3(\Delta h/h)^2} \tag{A3}$$

For the free-molecule regime, where $\bar{v}_r$ is proportional to $h\Delta P$, the equivalent expression to Eq. (A3) is

$$\frac{\Delta P_2}{\Delta P_1} = \frac{1}{1+(\Delta h/h)^2} \tag{A4}$$

Equations (A3) and (A4) show that the effect of displacing a shield from an evenly spaced position reduces the net pressure differential. Also, the effect is greater in the viscous regime than in the free-molecule regime. As layer density is increased and h is reduced by applying pressure to the sample, it seems reasonable to suppose that Δh would not be decreased as fast as h. Indeed, Δh may remain constant or even increase. Therefore, the fraction $\Delta h/h$, and hence the fractional reduction in differential pressure caused by a given change in spacing, should thus increase with increasing layer density.

Acknowledgments

This work was performed under Contract NAS 3-14377, NASA Lewis Research Center, under the technical direction of William R. Johnson.

References

[1]Glassford, A. P. M., "Prediction of Pressure during Evacuation of Multilayer Insulation," *Journal of Spacecraft and Rockets,* Vol. 9, May 1972, pp. 378-381.

[2]Keller, C. W., Cunnington, G. R., and Glassford, A. P. M., "Thermal Performance of Multilayer Insulations," NASA CR-134477/LMSC-D349866 (Final Report to NAS 3-14377), April 5, 1974.

[3]Loeb, L. B., *The Kinetic Theory of Gases,* 3rd ed., Dover, New York, 1961, p. 284.

[4]Dushman, S., *Foundations of Vacuum Techniques,* 2nd ed., Wiley, New York, 1962, Chap. 1, p. 87.

[5]Browne, V. d'A. and John, J. E. A., "Vacuum Radial Flow from the Viscous through the Free-Molecule Regime," *Vacuum,* Vol. 20, Dec. 1970, pp. 525-533.